ADVANCING EARTH AND SPACE SCIENCES

Geophysical Research Letters

RESEARCH LETTER
10.1029/2026GL121932

Key Points:

- Using THEMIS data, we report for the first time rising-tone EMIC waves driven by the impact of magnetosheath HSJ on the magnetopause
- Two rising-tone EMIC wave elements are generated during the magnetopause "Rebounce" phase, with distinct chirping rates and amplitudes
- Protons with higher energies and PAs rapidly replenish the equator, leading to a significant increase in flux and temperature anisotropy

Supporting Information:

Supporting Information may be found in the online version of this article.

Correspondence to:

X. Gao and X. Zhou,
gaoxl@ustc.edu.cn;
zhoux1@mail.ustc.edu.cn

Citation:

Lei, W., Gao, X., Zhou, X., Ma, J., Shao, T., Wang, Y., & Lu, Q. (2026). First report of rising-tone EMIC waves driven by the magnetosheath high-speed jet. *Geophysical Research Letters*, *53*, e2026GL121932. https://doi.org/10.1029/2026GL121932

Received 21 JAN 2026
Accepted 23 JUN 2026

First Report of Rising-Tone EMIC Waves Driven by the Magnetosheath High-Speed Jet

Wentian Lei[1,2], Xinliang Gao[1,2], Xuan Zhou[1,2], Jiuqi Ma[1,2], Tong Shao[1,2], Yuxiang Wang[1,2], and Quanming Lu[1,2]

[1]Deep Space Exploration Laboratory, School of Earth and Space Sciences, University of Science and Technology of China, Hefei, China, [2]CAS Center for Excellence in Comparative Planetology, Hefei, China

Abstract Magnetosheath high-speed jets (HSJs) are pervasive transient structures with enhanced dynamic pressure in the terrestrial magnetosheath and can exert notable local impacts on the magnetopause. Although various geoeffects have been reported to be associated with HSJs, whether HSJs can drive the generation of electromagnetic ion cyclotron (EMIC) waves remains unknown. Using coordinated observations from THEMIS-A and THEMIS-E, we report the first observation of magnetospheric EMIC waves driven by a HSJ. Two rising-tone EMIC wave elements are detected during the "Rebounce" phase of the magnetopause's response to the HSJ impact, exhibiting distinct chirping rates and magnetic amplitudes. During this phase, higher-energy protons with larger pitch angles efficiently replenish the magnetic equatorial region, leading to a significant increase in proton flux and temperature anisotropy. Both linear and nonlinear theoretical models confirm that these energetic protons account for the excitation of the observed rising-tone EMIC waves.

Plain Language Summary Magnetosheath high-speed jets (HSJs) are localized dynamic pressure enhancements that can frequently strike the boundary of Earth's dayside magnetic field (the magnetopause), triggering various space weather effects. However, it remained unclear whether they could drive the generation of electromagnetic ion cyclotron (EMIC) waves, a type of electromagnetic wave that strongly influences particle dynamics within the magnetosphere. In this study, using joint observations of THEMIS-A and E satellites, we report the first detection of EMIC waves driven by an HSJ. During the "Rebounce" phase of the magnetopause following the HSJ impact, two distinct rising-tone EMIC wave elements were observed, each exhibiting different chirping rates and wave amplitudes. Our analysis further shows that in this phase, higher-energy protons with larger pitch angles experience stronger magnetic mirror forces, enabling them to return more rapidly to the magnetic equatorial region. This leads to a pronounced increase in proton flux and temperature anisotropy, which supplies the free energy required for the EMIC wave growth. Our findings demonstrate for the first time that HSJs can drive the generation of EMIC waves in the magnetosphere, with important implications for understanding charged particle behavior in near-Earth space.

1. Introduction

High-speed jets (HSJs) are transient structures characterized by locally enhanced dynamic pressure, commonly observed in the magnetosheaths of Earth and other planets. Such enhancements arise primarily from the increased ion density, velocity, or a combination of both (Plaschke et al., 2018). Extensive studies have shown the foreshock-related phenomena at the quasi-parallel shock mainly contribute to the formation of the HSJs (Plaschke et al., 2013; Vuorinen et al., 2019). These mechanisms include bow shock surface ripples (Hao et al., 2016; Hietala & Plaschke, 2013), interactions between foreshock fluctuations and the bow shock (Raptis et al., 2022; Ren et al., 2023), and shock interactions with rotational discontinuities (Archer et al., 2012).

HSJs carrying large volumes of plasma directly impact the magnetopause, inducing magnetopause deformation. This effect is similar to that of the solar wind, though it occurs on a far smaller spatial scale (Guo et al., 2022; Ren et al., 2024). The comprehensive response of magnetopause to HSJ can be described by a "Compression-Rebounce-Relaxation" sequence (J. Ma et al., 2024). Such localized impact drives several potential consequences: local indentations of the magnetosphere, the generation of surface and compressional waves (including ultra-low frequency waves; Archer et al., 2014; B. Wang et al., 2022), and localized magnetopause reconnection (Hietala et al., 2018). This process is also linked to dayside ionospheric flow enhancements (Hietala et al., 2012) and ground-observed throat auroral brightening (B. Wang et al., 2018; Z. Wang et al., 2025).

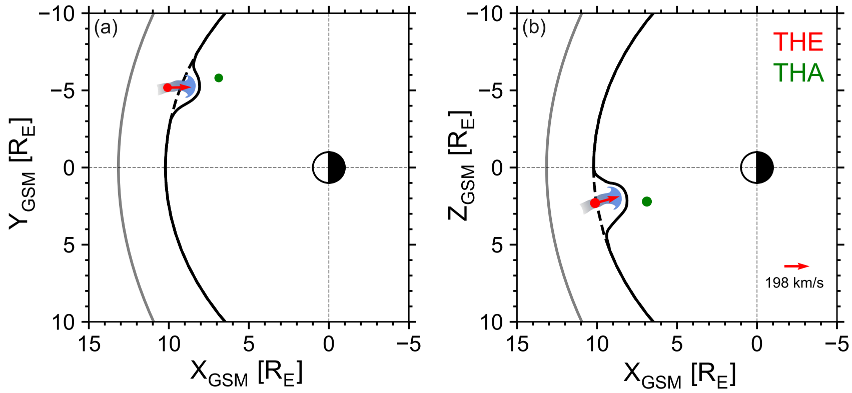

Figure 1. The position of THEMIS-A (green) and THEMIS-E (red) in x-y (a) and x-z (b) planes in the geocentric solar magnetospheric (GSM) coordinate system at 10:45 UT on 8 February 2013. The red arrow indicates the ion velocity vector corresponding to the peak dynamic pressure.

Recently, using the combined observations from THEMIS-A and THEMIS-E observations, Zhou et al. (2024) uncovered the role of HSJs in regulating the whistler-mode chorus waves in the magnetosphere. They found that HSJ compression induces a sharp drop in electron flux, which in turn results in the rapid disappearance of chorus waves. Electromagnetic ion cyclotron (EMIC) waves, another common plasma wave in the magnetosphere, are well known for efficiently scattering relativistic electrons and facilitating ring current decay (Capannolo et al., 2019; Fraser et al., 2010; Q. Ma et al., 2025; Thorne, 2010; Zhang et al., 2016). EMIC waves share several similarities with whistler-mode chorus waves: like chorus waves, they are generated by the temperature anisotropy of charged particles, and their excitation can also be driven by solar wind-induced magnetopause compression (Chen et al., 2020; Jun et al., 2024; McCollough et al., 2012). This raises a critical question: can HSJ impacts modulate EMIC wave generation?

In this study, utilizing joint observations from THEMIS-A and THEMIS-E, we report for the first time the generation of rising-tone EMIC waves driven by a magnetosheath HSJ. Two rising-tone EMIC wave elements are detected during the "Rebounce" phase of the magnetopause response to the HSJ impact, and not during the "Compression" phase. Both wave elements display clear and distinct frequency chirping rates. During the "Rebounce" phase, higher-energy protons with larger pitch angles efficiently replenish the magnetic equatorial region, which in turn gives rise to a substantial enhancement in proton flux and temperature anisotropy. Based on both linear and nonlinear theoretical frameworks, we confirm that these energized protons serve as the primary driver for the excitation of EMIC waves.

2. Instruments and Data

The THEMIS mission, consisting of five nearly identically instrumented probes (THEMIC-A, B, C, D, and E), was launched in February 2007. Since 2011, three of them, that is, THEMIS-A, D, and E, have remained in Earth orbit with their apogees exceeding 10 R_E and perigees below 2 R_E. They not only provide ideal coverage of the source region (magnetic equator) for plasma waves in the magnetosphere, but also offer an excellent opportunity for joint observations of dayside magnetosheath and magnetosphere. The onboard flux gate magnetometer (FGM) records the background magnetic field and its low frequency fluctuations up to 64 Hz, which can be used to analyze EMIC waves. The electrostatic analyzer (ESA) and solid-state telescope (SST) measure ion distribution functions across complementary energy ranges: ESA covers energies from a few eV to 25 keV, while SST extends measurements up to 6 MeV. Plasma density is inferred from two quantities: the spacecraft potential, measured by electric field instrument (EFI), and thermal velocity, measured by ESA. Solar wind data are obtained from the OMNI website (https://omniweb.gsfc.nasa.gov) with 1-min resolution, and have been time-shifted to Earth's bow shock nose.

3. Observational Results

During the time interval of 10:35–10:55 UT on 8 February 2013, THEMIS-A and THEMIS-E were operating on opposite sides of the magnetopause, enabling coordinated observations of the HSJ impact. Figures 1a and 1b

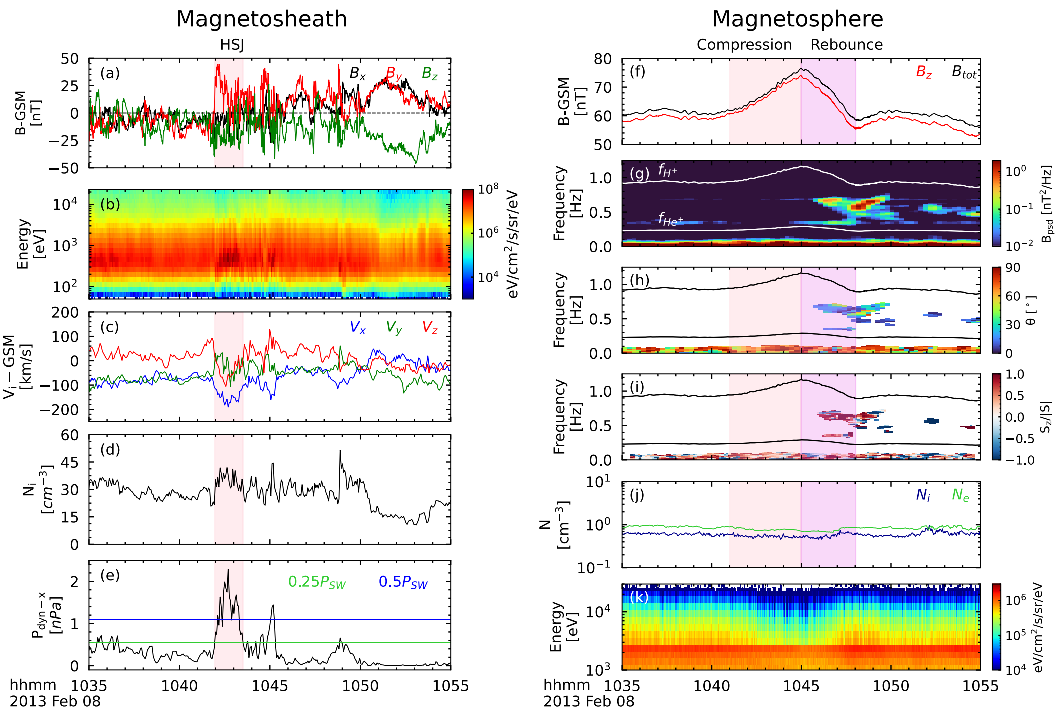

Figure 2. The overview of a high-speed jet in the magnetosheath observed by THEMIS-E (a–e), and the response in the magnetosphere detected by THEMIS-A (f–k) from 10:35 to 10:55 UT on 8 February 2013. (a) The magnetic field in GSM coordinate system. (b) Ion energy flux. (c) Ion bulk velocity in the GSM coordinate system. (d) Ion density. (e) X component ion dynamic pressure ($P_{\text{dyn-x}}$) in GSM coordinate system at THEMIS-E in black; corresponding solar wind data ($P_{\text{sw-x}}/2, P_{\text{sw-x}}/4$) are shown in blue and green. (f) The geomagnetic field in magnetosphere (B_{tot}, black line), and its z-direction component (B_z, red line). (g) The wave magnetic power spectral density (B_{psd}). (h) The wave normal angle relative to the background magnetic field. (i) The ratio $S_z/|S|$, where S is the Poynting flux intensity and S_z is its parallel component along B_0. (j) Background electron density and ion density. (k) Ion energy flux. The solid lines in panels (g–i) represent f_{H^+} and f_{He^+}.

depict their locations (THEMIS-A in green, THEMIS-E in red) at 10:45 UT in the geocentric solar magnetospheric (GSM) coordinate system, projected onto the X-Y and X-Z planes, respectively. The bow shock (gray line) and magnetopause (black line) are also plotted for reference, based on the model by Shue et al. (1998). The red arrow denotes the ion velocity vector of the HSJ at the time of its dynamic pressure maximum. Both spacecraft were located on the morning side (MLT $\approx$ 9 hr) and near the magnetic equator. The separation distances between them are approximately 3.2 R_E along the X direction, 0.6 R_E along the Y direction, and 0.1 R_E along the Z direction. The HSJ firstly encountered THEMIS-E in the magnetosheath with the bulk velocity of $\sim$198 km/s, and then it propagated nearly directly toward THEMIS-A. Approximately 2 min later, THEMIS-A detected the signal of the HSJ impacting the magnetopause inside the magnetosphere.

Figures 2a–2e present the magnetic field and plasma measurements from THEMIS-E during the interval of interest. Here, in Figure 2e, the X component of dynamic pressure $P_{\text{dyn-x}}$ is defined as $N_i m_p V_{ix}^2$ (m_p is the proton mass), and the blue and green lines mark the half and the quarter of solar wind dynamic pressure ($P_{\text{SW}} \approx 2.3$ nPa, after a 1-hr time shift and a 20-min running average). The observations exhibit typical magnetosheath characteristics, including a turbulent magnetic field with magnitudes ranging from a few nT to 50 nT (Figure 2a) and ion fluxes that are predominantly distributed between 100 eV and 2 keV (Figure 2b). Two HSJs are recorded by THEMIS-E, identified by their $P_{\text{dyn-x}}$ peaks well above the blue line in Figure 2e, due to enhancements in both ion density (Figure 2d) and bulk velocity (Figure 2c). Here, we focus on the stronger HSJ shaded in pink, which propagated primarily in the X-direction ($v_x \approx 190$ km s^{-1}, $v_y \approx 4$ km s^{-1}, $v_z \approx 55$ km s^{-1}; Figure 2c). Its dynamic pressure peaks at $\sim$2.2 nPa, a value sufficient to induce a noticeable magnetopause indentation. Additionally, a bow wave precedes this HSJ ($\sim$10:42 UT), characterized by localized enhancements in magnetic field and ion density (Figures 2a and 2d). During the relevant interval, substorm activity, as indicated by the AE/AL indices, was confined to 06:30–09:00 UT and absent during our wave event (10:30–10:55 UT). Meanwhile, the solar wind

10.1029/2026GL121932

dynamic pressure remained stably around ∼2.3 nPa. We also calculated the drift time of protons injected during strong substorm activity and found that the substorm-related protons could not affect the EMIC waves observed at 10:46:30 UT. These results rule out both substorm injections and solar wind pressure enhancements as the source of the observed EMIC waves. The full temporal evolution supporting this conclusion is detailed in Figure S1 of Supporting Information S1.

The magnetospheric response to the HSJ is shown in Figures 2f–2k, based on THEMIS-A observations in the inner magnetosphere ($\mathrm{L} - \mathit{Shell} = 9.2$) and near the dawn side geomagnetic equator ($\mathrm{MLT} = 9.4\ hr$ and $\mathrm{MLAT} = 1.8°$). Starting at ∼10:41 UT, the geomagnetic field exhibits a clear compressional signal, as B_z (in GSM coordinates, red line) and B_{tot} (black line) increase by more than 4 nT per minute, reaching a maximum enhancement of ∼15 nT at 10:45 UT (Figure 2f). This interval corresponds to the "Compression" phase of the magnetopause response (shaded in pink). Following this, the magnetopause enters the "Rebounce" phase (shaded in purple), continuing until ∼10:48 UT, leading to a significant decrease in the total magnetic field to ∼58 nT, even weaker than the magnetic field preceding the HSJ impact. During this short interval (∼5 min), the displacement of THEMIS-A is less than 0.1 R_E, far smaller than the HSJ's spatial scale. Therefore, the observed magnetic field variations reliably reflect the magnetospheric response to the HSJ impact rather than any artifact of satellite motion. Moreover, the end of "Compression" phase of the magnetopause response is delayed by about 90 s relative to the trailing edge of the HSJ observed in the magnetosheath, consistent with a simple estimation (∼108s) calculated by dividing the along-X separation between two spacecraft $\left(\Delta x \sim 3.2\ R_E\right)$ by the V_{ix} of the HSJ $\left(V_{ix}\ \approx\ 190\ \mathrm{km\ s^{-1}}\right)$. Therefore, it is reasonable to conclude that the variation of the magnetic field is driven by the HSJ's impact on the magnetopause.

During the "Rebounce" phase, two rising-tone EMIC wave elements are detected by THEMIS-A in the magnetosphere (Figure 2g). The first wave element, identified as proton-band EMIC waves, initiates at an initial frequency of ∼0.65 Hz and exhibits a mild frequency chirping trend from 10:46:15 to 10:47:00 UT, with a chirping rate of $\Gamma_1 = 6.98 \times 10^{-3}\ \mathrm{rad\ s^{-2}}$. Their wave normal angle is generally less than 30° (Figure 2h), with coexisting parallel (red) and antiparallel (blue) Poynting fluxes indicative of proximity to the source region (Figure 2i). The second rising-tone EMIC wave element (also proton-band) is triggered precisely at the end of the "Rebounce" phase with a larger chirping rate of $\Gamma_2 = 9.92 \times 10^{-3}\ \mathrm{rad\ s^{-2}}$. They exhibit a similar wave normal angle and propagation direction to the first element (Figures 2h and 2i), but substantially larger wave amplitude (Figure 2g).

The response of proton flux strongly depends on proton energy (Figure 2k). Lower-energy protons (<1 keV), which mainly contribute to the plasma density, remain nearly unchanged during the entire time interval (Figures 2j and 2k). In contrast, higher-energy protons, particularly those with energies >5 keV, experience a rapid flux decrease during the "Compression" phase (Figure 2k); a similar response is observed for energetic electrons (not shown). The flux drop is driven by the local indentation of magnetopause following the HSJ impact. This indentation leads to the formation of a new magnetic mirror point at the equator, with some particles subsequently expelled by the mirror force (Zhou et al., 2024). During the "Rebounce" phase, the flux of energetic protons exhibits a rapid increase, as the previously expelled protons can return to the magnetic equator, even exceeding the flux preceding the HSJ impact by the end of this phase (Figure 2k). We speculate that the excitation of rising-tone EMIC waves results from enhanced proton fluxes during the "Rebounce" phase.

We further exhibit the pitch angle distributions of protons at two typical energies (i.e., 3 and 25 keV) above the minimum resonant energy (1.57 keV) of EMIC waves at 0.6 Hz in Figures 3b and 3c. This minimum resonant energy is derived from the cyclotron resonance condition, $m_p(\omega - \Omega_p)^2/2k_{\|}^2$, where m_p is the proton mass, Ω_p is proton gyrofrequency, ω is the wave frequency and $k_{\|}$ is the parallel wave number derived from cold plasma approximation (Baumjohann & Treumann, 2022). Figure 3d shows the time profiles of proton flux for the two selected energy channels. Figure 3e presents the evolution of temperature anisotropy, which is estimated as the ratio of ion flux at 78.75° pitch angle to that at 11.25° pitch angle for each energy channel. As shown in Figures 3b and 3c, both 3 keV and 25 keV proton fluxes undergo a sharp decrease during the "Compression" phase and a rapid increase during the "Rebounce" phase across all pitch angles. Concurrently, the flux evolution in Figure 3d exhibits a similar trend, but with more pronounced changes observed for higher-energy (25 keV) protons.

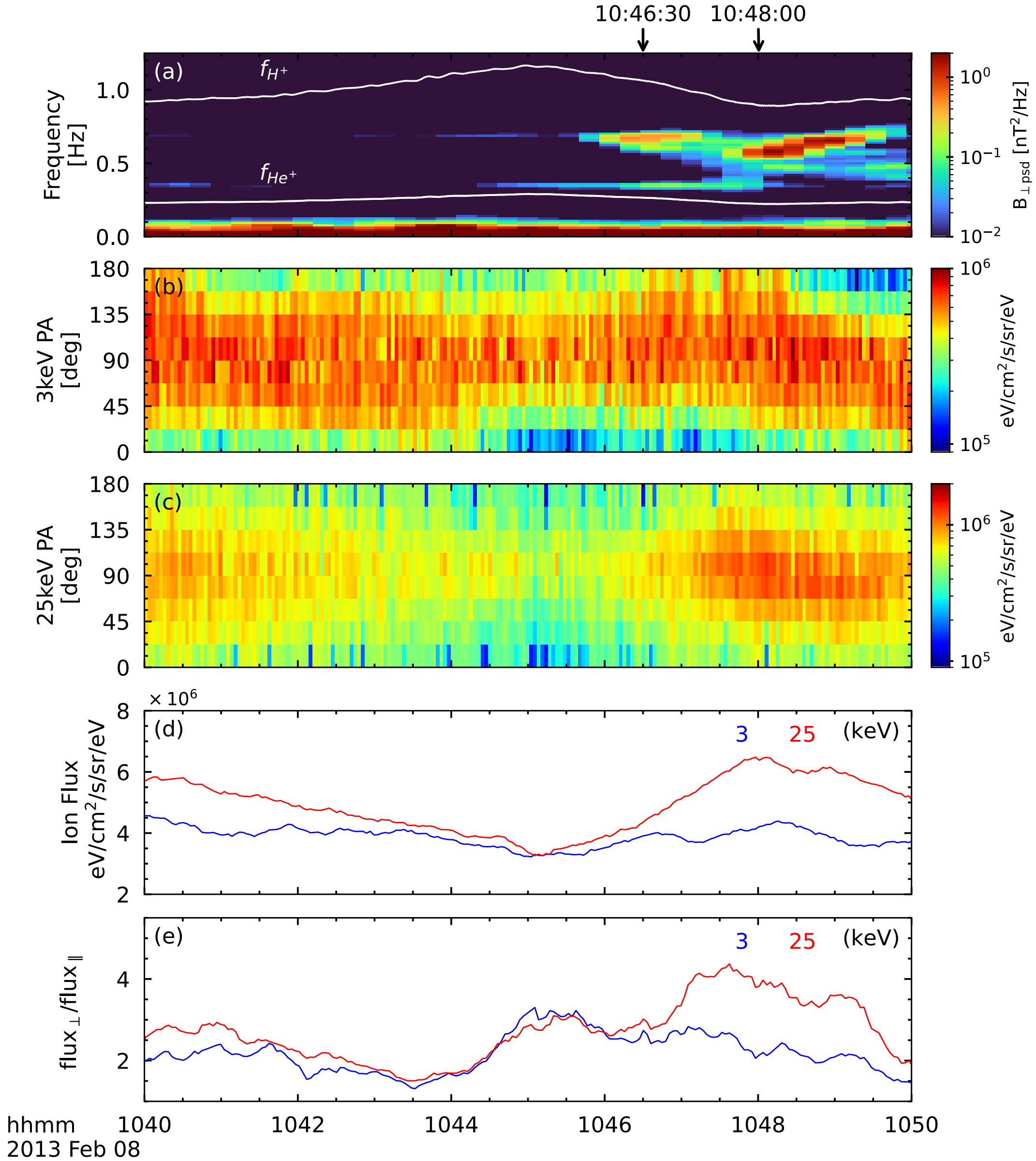

Figure 3. The evolution of ion pitch angle distributions at selected energies in the magnetosphere detected by THEMIS-A. (a) Magnetic power spectral density, for context. (b, c) Ion pitch angle distributions for 3 and 25 keV protons. (d) Ion flux for 3 and 25 keV protons. (e) The ratio of ion flux at pitch angle 78.75° to that at 11.25°.

Surprisingly, we also find that proton flux variations depend on pitch angle, which gives rise to a complex response of temperature anisotropy to HSJ impact (Figure 3e). At the early stage of the "Compression" phase, both parallel and perpendicular fluxes decrease with a stronger reduction in the perpendicular direction. This leads to a gradual decrease in temperature anisotropy, despite betatron heating being operative here due to the continuous compression of the ambient magnetic field. After ~10:43:30 UT, however, the betatron heating mitigates the decline in perpendicular flux, causing temperature anisotropy to increase until the end of the "Compression" phase. During the "Rebounce" phase, both parallel and perpendicular fluxes start to increase (Figure 3d), but temperature anisotropy initially decreases slowly primarily due to the betatron cooling effect. Although betatron cooling operates throughout the "Rebounce" phase, the perpendicular flux recovers faster than parallel flux starting at ~10:46 UT, when coincides with the growth of the first rising-tone EMIC wave element. By the end of the "Rebounce" phase, both proton flux and temperature anisotropy reach their maxima, which coincides with the excitation of the second rising-tone EMIC waves element.

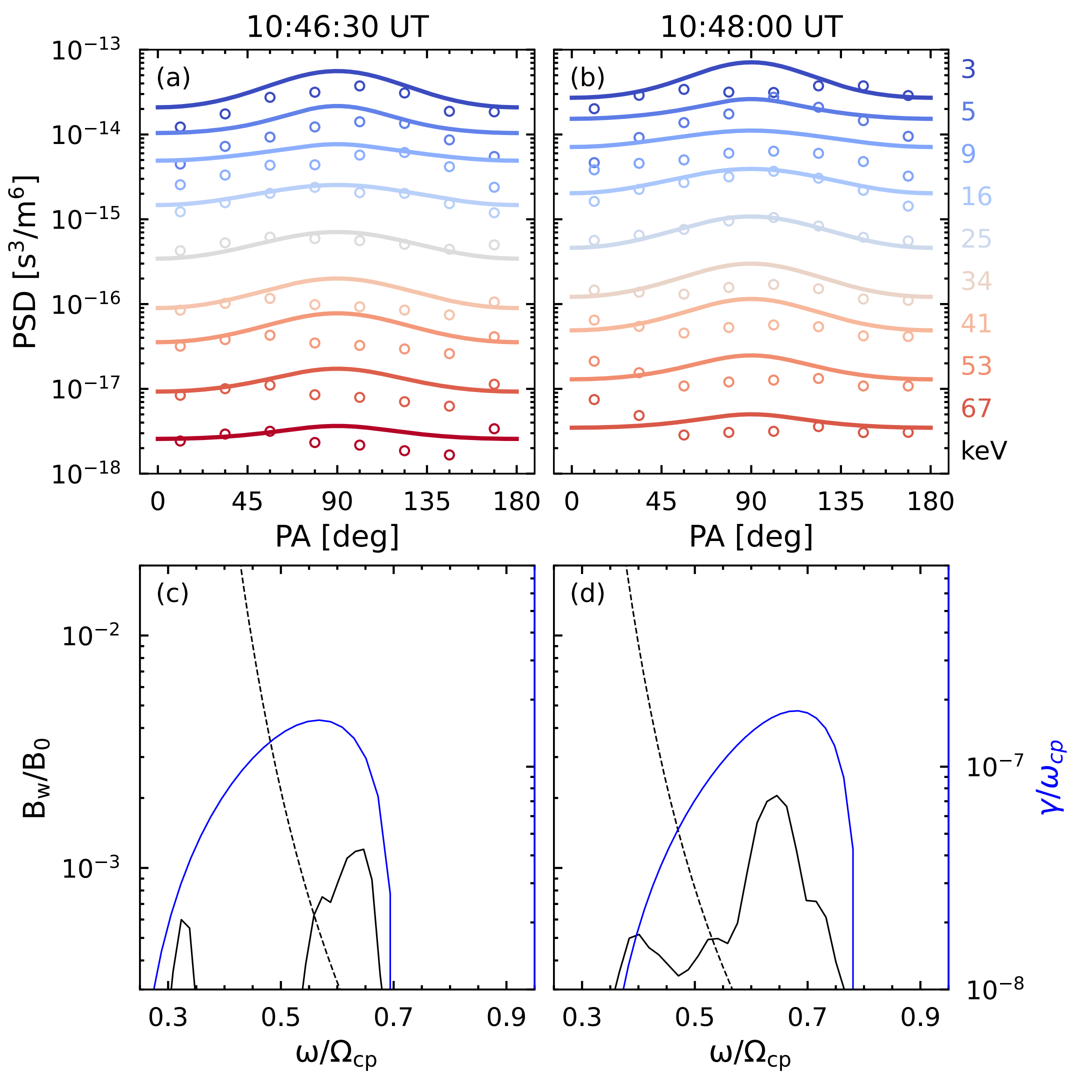

Figure 4. (a, b)Observed (circles) and fitted proton phase space densities at 10:46:30 UT and 10:48:00 UT, (c, d) the wave amplitudes (black solid line); nonlinear threshold amplitudes (black dashed line, Q = 1); linear growth rate (blue line) at 10:46:30 UT and 10:48:00 UT.

To confirm that the generation of EMIC waves arises from the evolution of energetic protons during the HSJ impact, we have selected two time points (10:46:30 and 10:48:00 UT marked by arrows on the top of Figure 3) corresponding to the start of rising tones, to calculate the linear growth rate and nonlinear threshold amplitude. Figures 4a and 4b present the pitch-angle distributions (circles) of protons measured by THEMIS-A at the two time points. The observed distributions are fitted to a multi-component bi-Maxwellian distribution:

$$f(v_{\parallel},\ v_{\perp}) = \sum_j \sqrt{\frac{m}{2T_{\parallel j}\pi}}\ \frac{m}{2T_{\perp j}\pi} n_j \exp\left(-\frac{mv_{\parallel}^2}{2T_{\parallel}} - \frac{mv_{\perp}^2}{2T_{\perp}}\right) \tag{1}$$

where m, n_j, $T_{\parallel j}$, $T_{\perp j}$ are mass, number density, parallel and perpendicular temperature of the j component, respectively. The fitted distributions are plotted as solid lines in Figures 4a and 4b, which are in good agreement with the observations. The detailed fitting parameters, which serve as input parameters for linear theoretical models (e.g., the BO model), are provided in Table S1 of Supporting Information S1. The calculated linear growth rates (blue lines) and wave amplitudes (black lines) at the two time points are presented in Figures 4c and 4d. The frequency range ($\sim 0.3 - 0.7\ \Omega_p$) of positive linear growth rates well covers the wave spectra, and the peak frequencies of linear growth rates aligns closely with those of the wave amplitudes. These results support the local excitation of EMIC waves during the "Rebounce" phase.

Then, we employ a widely used parabolic approximation for the background magnetic field, $B = B_0(1 + ah^2)$, where a is a key parameter characterizing magnetic field inhomogeneity, and h is the distance along a field line from the magnetic equator. The values of a are determined using TS04 geomagnetic field model (Tsyganenko & Sitnov, 2005) by requiring that the resulting B_z profile and the B_z/B ratio agree well with in situ satellite observations, which yields $a \approx 2.12 \times 10^{-15}\ \mathrm{m}^{-2}$ at 10:46:30 UT and $a \approx 2.48 \times 10^{-15}\ \mathrm{m}^{-2}$ at 10:48:00 UT. Following the formulation outlined by Omura et al. (2010), the theoretical chirping rate and threshold amplitude are expressed as:

$$\frac{\partial \omega}{\partial t} = \frac{0.4 s_0 \omega}{s_1} \Omega_w \tag{2}$$

$$\tilde{B}_{\mathrm{th}} = \frac{100\pi^3 \tilde{V}_p^3}{\tilde{\omega}\tilde{\omega}_{ph}^4 \tilde{V}_\perp^5} \left(\frac{\tilde{a} s_2 \tilde{V}_\parallel}{Q}\right)^2 \exp\left(\frac{\tilde{V}_R^2}{\tilde{V}_\parallel^2}\right) / B_0 \tag{3}$$

where

$$s_0 = \frac{V_\perp}{V_p} \tag{4}$$

$$s_1 = \left(1 - \frac{V_R}{V_g}\right)^2 \tag{5}$$

$$s_2 = \left(\frac{V_\perp^2}{2V_p^2} + \frac{V_R^2}{V_p V_g} - \frac{V_R^2}{2V_p^2}\right)\frac{\omega}{\Omega_p} - \frac{V_R}{V_p} \tag{6}$$

and $\Omega_w = eB_w/m_H$. Here, ω and k denote the wave angular frequency and wavenumber; V_g, V_p and V_R represent the wave group velocity, phase velocity and resonance velocity of protons, $V_\parallel$ and $V_\perp$ are the proton parallel and perpendicular velocity at the magnetic equator, which are estimated by the component 4 in Table S1 of Supporting Information S1 via Liouville's theorem, respectively. The tilde variables are normalized by the speed of light c and the equatorial proton gyrofrequency Ω_{p0}.The threshold amplitudes for the nonlinear wave growth are overplotted as dashed lines in Figures 4c and 4d. It is clearly shown that the amplitudes of higher-frequency (⟩$0.55\ \Omega_{p0}$) EMIC waves at the two time points exceeds the threshold, accounting for the observed frequency chirping. In contrast, their lower-frequency counterparts fail to transition into the nonlinear regime, as their amplitudes remain below the threshold. Furthermore, we estimate the theoretical chirping rates at these two time points as $\Gamma_1' = 4.17 \times 10^{-3}$ rad s^{-2} and $\Gamma_2' = 5.85 \times 10^{-3}$ rad s^{-2}, yielding a ratio of $\Gamma_1'/\Gamma_2' \approx 1.4$. Considering that uncertainties in plasma parameters may introduce a factor of two uncertainty in chirping rate calculations, the observed frequency chirping rates ($\Gamma_1 = 6.98 \times 10^{-3}$ rad s^{-2} and $\Gamma_2 = 9.92 \times 10^{-3}$ rad s^{-2}) are in good agreement with the theoretical values, particular their ratio ($\Gamma_1/\Gamma_2 \approx 1.41$). We thus conclude that the proton distribution reshaped by the HSJ impact facilitate the excitation of rising-tone EMIC waves.

4. Conclusion and Discussion

In this study, based on coordinated observations from THEMIS-A and THEMIS-E, we present the first observational report of magnetospheric EMIC waves driven by HSJs. A HSJ firstly encountered by THEMIS-E in the magnetosheath, triggering a comprehensive magnetospheric response, that is, subsequently captured by THEMIS-A. This magnetospheric response to the HSJ is characterized by a "Compression-Rebounce-Relaxation" sequence, as illustrated in Figure S2 of Supporting Information S1. During the "Compression" phase, a clear enhancement in the geomagnetic field was detected. This localized compression induces the formation of a new magnetic mirror point near the equator. The energetic protons were expelled by the mirror force, which results in a significant flux drop. In the subsequent "Rebounce" phase, the local geomagnetic field gradually decreased, eventually falling to a level even lower than that preceding the HSJ impact. During this phase, two rising-tone EMIC wave elements are excited, and they exhibit distinct chirping rates and magnetic amplitudes. Higher-energy protons with larger pitch angles experience a larger mirror force, which efficiently replenish the magnetic equatorial region. This leads to a significant increase in proton flux and temperature anisotropy, which provides the sufficient free energy for the EMIC wave growth. Both linear and nonlinear theoretical analyses confirm that these energetic protons are responsible for the local excitation of the observed rising-tone EMIC waves. This study thus provides the first compelling evidence that HSJs can regulate the generation of EMIC waves in the magnetosphere. Given that EMIC waves play a key role in scattering relativistic electrons and ring current protons, we suggest that HSJs can potentially regulate magnetospheric particle dynamics via magnetopause interactions.

The response of proton dynamics to the HSJ impact is found to be critically dependent on both the pitch angle and energy. As shown in Figures 2k and 3c, protons with larger energies and pitch angles respond more efficiently and rapidly to HSJ-driven perturbations. Based on the mirror force equation $F_m = -\mu \nabla_{\parallel} B$ (where $\mu = \left(m v_{\perp}^2\right)/2B$ denotes the first adiabatic invariant), we can readily rationalize that they experience a stronger mirror force, amplifying their sensitivity to magnetic field variations and further enhancing response efficiency. Meanwhile, betatron heating/cooling also acts on these protons, with its effect equally dependent on pitch angle and energy. These two mechanisms participate in modulating the evolution of temperature anisotropy during distinct phases of the magnetopause response to HSJs. During the early "Compression" phase or late "Rebounce" phase, the flux of high-energy protons at pitch angles from 45° to 135° undergoes more pronounced decreases or increases due to the mirror force, driving corresponding reductions or enhancements in temperature anisotropy. In contrast, during the late "Compression" phase or early "Rebounce" phase, betatron heating or cooling dominates, accounting for the observed increase or decrease in temperature anisotropy. For the EMIC waves with resonate energy well above 1 keV, HSJs create the necessary plasma conditions to drive the excitation of magnetospheric EMIC waves by reshaping the proton velocity distribution function during their interaction with the magnetosphere.

The observed field inhomogeneity variation originates from the HSJ-induced localized magnetic field deformation. During the "Rebounce" phase, this restructuring proceeds in a two-stage evolution. At first, magnetic field lines start to rebound, leading to the vanishing of the newly formed magnetic mirror point and a reduction in local field inhomogeneity. In the subsequent stage, continued magnetic field line rebound causes the local magnetic field strength to decrease continuously until it reaches its minimum, driving a corresponding rise in magnetic field inhomogeneity. For the second EMIC wave element, the local magnetic field has reached its minimum, corresponding to the peak of magnetic field inhomogeneity. Since the nonlinear threshold is positively correlated with magnetic field inhomogeneity (Equation 3), we conclude that the enhanced particle flux and temperature anisotropy (i.e., increased free energy) lead to the nonlinear excitation of this wave element. For the first element, the reduction in magnetic field inhomogeneity may facilitate the nonlinear wave growth. However, the calculated chirping rates (governed by the proton free energy) are in quantitative agreement with the observational results (Omura et al., 2010). We thus clarify that proton dynamics serve as the dominant driver of EMIC wave nonlinear growth. Notably, recent theoretical studies have demonstrated a strong dependence of the chirping rate on background magnetic field inhomogeneity, that is, evaluated at the wave source location upstream of the magnetic equator (An et al., 2024; Tao et al., 2021). However, single-satellite observations and a steady-field model are inherently limited in tracking wave evolution. A detailed verification of the evolving localized magnetic field structure and associated particle dynamics will be performed in the future work using self-consistent numerical simulations.

Conflict of Interest

The authors declare no conflicts of interest relevant to this study.

Availability Statement

The observational data from THEMIS are available from the website https://themis.ssl.berkeley.edu/data/themis/. The OMNI data are obtained from the website http://spdf.gsfc.nasa.gov/pub/data/omni/.

Geophysical Research Letters 10.1029/2026GL121932

Acknowledgments

This research was funded by National Key Research and Development Program of China (2025YFF0512500 and 2022YFA1604600), the NSFC Grants 42322406 and 42230201, the "USTC Tang Scholar" program, and the Fundamental Research Funds for the Central Universities (KY2080000063 and KY2080000138). We also acknowledge the entire THEMIS instrument team.

References

An, Z., Tao, X., Zonca, F., & Chen, L. (2024). Frequency chirping of electromagnetic ion cyclotron waves in Earth's magnetosphere. *Geophysical Research Letters*, *51*(4), e2023GL106456. https://doi.org/10.1029/2023GL106456

Archer, M. O., Horbury, T. S., & Eastwood, J. P. (2012). Magnetosheath pressure pulses: Generation downstream of the bow shock from solar wind discontinuities. *Journal of Geophysical Research*, *117*(A5). https://doi.org/10.1029/2011JA017468

Archer, M. O., Turner, D. L., Eastwood, J. P., Horbury, T. S., & Schwartz, S. J. (2014). The role of pressure gradients in driving sunward magnetosheath flows and magnetopause motion. *Journal of Geophysical Research: Space Physics*, *119*(10), 8117–8125. https://doi.org/10.1002/2014JA020342

Baumjohann, W., & Treumann, R. A. (2022). *Basic space plasma physics* (3rd ed.). World Scientific. https://doi.org/10.1142/12771

Capannolo, L., Li, W., Ma, Q., Shen, X.-C., Zhang, X.-J., Redmon, R. J., et al. (2019). Energetic electron precipitation: Multievent analysis of its spatial extent during emic wave activity. *Journal of Geophysical Research: Space Physics*, *124*(4), 2466–2483. https://doi.org/10.1029/2018JA026291

Chen, H., Gao, X., Lu, Q., Tsurutani, B. T., & Wang, S. (2020). Statistical evidence for emic wave excitation driven by substorm injection and enhanced solar wind pressure in the earth's magnetosphere: Two different emic wave sources. *Geophysical Research Letters*, *47*(21), e2020GL090275. https://doi.org/10.1029/2020GL090275

Fraser, B. J., Grew, R. S., Morley, S. K., Green, J. C., Singer, H. J., Loto'aniu, T. M., & Thomsen, M. F. (2010). Storm time observations of electromagnetic ion cyclotron waves at geosynchronous orbit: Goes results. *Journal of Geophysical Research*, *115*(A5). https://doi.org/10.1029/2009JA014516

Guo, J., Lu, S., Lu, Q., Lin, Y., Wang, X., Ren, J., et al. (2022). Large-scale high-speed jets in Earth's magnetosheath: Global hybrid simulations. *Journal of Geophysical Research: Space Physics*, *127*(6), e2022JA030477. https://doi.org/10.1029/2022JA030477

Hao, Y., Lembege, B., Lu, Q., & Guo, F. (2016). Formation of downstream high-speed jets by a rippled nonstationary quasi-parallel shock: 2-D hybrid simulations. *Journal of Geophysical Research: Space Physics*, *121*(3), 2080–2094. https://doi.org/10.1002/2015JA021419

Hietala, H., Phan, T. D., Angelopoulos, V., Oieroset, M., Archer, M. O., Karlsson, T., & Plaschke, F. (2018). In situ observations of a magnetosheath high-speed jet triggering magnetopause reconnection. *Geophysical Research Letters*, *45*(4), 1732–1740. https://doi.org/10.1002/2017GL076525

Hietala, H., & Plaschke, F. (2013). On the generation of magnetosheath high–speed jets by bow shock ripples. *Journal of Geophysical Research: Space Physics*, *118*(11), 7237–7245. https://doi.org/10.1002/2013JA019172

Hietala, H., Partamies, N., Laitinen, T. V., Clausen, L. B. N., Facskó, G., Vaivads, A., et al. (2012). Supermagnetosonic subsolar magnetosheath jets and their effects: From the solar wind to the ionospheric convection. *Annals of Geophysics*, *30*(1), 33–48. https://doi.org/10.5194/angeo-30-33-2012

Jun, C.-W., Miyoshi, Y., Nakamura, S., Shoji, M., Hori, T., Bortnik, J., et al. (2024). A triggering process for nonlinear emic waves driven by the compression of the dayside magnetosphere. *Geophysical Research Letters*, *51*(1), e2023GL106860. https://doi.org/10.1029/2023GL106860

Ma, J., Tang, B., Gao, X., Li, W., Lu, Q., Guo, W., et al. (2024). The comprehensive response of the magnetopause to the impact of an isolated magnetosheath high-speed jet. *Geophysical Research Letters*, *51*(21), e2024GL111132. https://doi.org/10.1029/2024GL111132

Ma, Q., Li, W., Bortnik, J., Hanzelka, M., Gan, L., Artemyev, A. V., & Shen, X.-C. (2025). Diffusive and nonlinear scattering of ring current protons by electromagnetic ion cyclotron waves in the earth's inner magnetosphere. *Journal of Geophysical Research: Space Physics*, *130*(8), e2025JA034078. https://doi.org/10.1029/2025JA034078

McCollough, J. P., Elkington, S. R., & Baker, D. N. (2012). The role of Shabansky orbits in compression-related electromagnetic ion cyclotron wave growth. *Journal of Geophysical Research*, *117*(A1). https://doi.org/10.1029/2011JA016948

Omura, Y., Pickett, J., Grison, B., Santolik, O., Dandouras, I., Engebretson, M., et al. (2010). Theory and observation of electromagnetic ion cyclotron triggered emissions in the magnetosphere. *Journal of Geophysical Research*, *115*(A7). https://doi.org/10.1029/2010JA015300

Plaschke, F., Hietala, H., & Angelopoulos, V. (2013). Anti-sunward high-speed jets in the subsolar magnetosheath. *Annals of Geophysics*, *31*(10), 1877–1889. https://doi.org/10.5194/angeo-31-1877-2013

Plaschke, F., Hietala, H., Archer, M., Blanco-Cano, X., Kajdič, P., Karlsson, T., et al. (2018). Jets downstream of collisionless shocks. *Space Science Reviews*, *214*(5), 81. https://doi.org/10.1007/s11214-018-0516-3

Raptis, S., Karlsson, T., Vaivads, A., Pollock, C., Plaschke, F., Johlander, A., et al. (2022). Downstream high-speed plasma jet generation as a direct consequence of shock reformation. *Nature Communications*, *13*(1), 598. https://doi.org/10.1038/s41467-022-28110-4

Ren, J., Guo, J., Lu, Q., Lu, S., Gao, X., Ma, J., & Wang, R. (2024). Honeycomb-like magnetosheath structure formed by jets: Three-dimensional global hybrid simulations. *Geophysical Research Letters*, *51*(12), e2024GL109925. https://doi.org/10.1029/2024GL109925

Ren, J., Lu, Q., Guo, J., Gao, X., Lu, S., Wang, S., & Wang, R. (2023). Two-dimensional hybrid simulations of high-speed jets downstream of quasi-parallel shocks. *Journal of Geophysical Research: Space Physics*, *128*(8), e2023JA031699. https://doi.org/10.1029/2023JA031699

Shue, J.-H., Song, P., Russell, C. T., Steinberg, J. T., Chao, J. K., Zastenker, G., et al. (1998). Magnetopause location under extreme solar wind conditions. *Journal of Geophysical Research*, *103*(A8), 17691–17700. https://doi.org/10.1029/98JA01103

Tao, X., Zonca, F., & Chen, L. (2021). A "trap-release-amplify" model of chorus waves. *Journal of Geophysical Research: Space Physics*, *126*(9), e2021JA029585. https://doi.org/10.1029/2021JA029585

Thorne, R. M. (2010). Radiation belt dynamics: The importance of wave-particle interactions. *Geophysical Research Letters*, *37*(22). https://doi.org/10.1029/2010GL044990

Tsyganenko, N. A., & Sitnov, M. I. (2005). Modeling the dynamics of the inner magnetosphere during strong geomagnetic storms. *Journal of Geophysical Research*, *110*(A3). https://doi.org/10.1029/2004JA010798

Vuorinen, L., Hietala, H., & Plaschke, F. (2019). Jets in the magnetosheath: IMF control of where they occur. *Annals of Geophysics*, *37*(4), 689–697. https://doi.org/10.5194/angeo-37-689-2019

Wang, B., Nishimura, Y., Hietala, H., & Angelopoulos, V. (2022). Investigating the role of magnetosheath high-speed jets in triggering dayside ground magnetic ultra-low frequency waves. *Geophysical Research Letters*, *49*(22), e2022GL099768. https://doi.org/10.1029/2022GL099768

Wang, B., Nishimura, Y., Hietala, H., Lyons, L., Angelopoulos, V., Plaschke, F., et al. (2018). Impacts of magnetosheath high-speed jets on the magnetosphere and ionosphere measured by optical imaging and satellite observations. *Journal of Geophysical Research: Space Physics*, *123*(6), 4879–4894. https://doi.org/10.1029/2017JA024954

Wang, Z., Han, D., Chen, X., Shi, R., Teng, S., Zhang, J., et al. (2025). Observations of a throat aurora directly driven by magnetosheath high-speed jet. *Journal of Geophysical Research: Space Physics*, *130*(1), e2024JA033276. https://doi.org/10.1029/2024JA033276

Zhang, X.-J., Li, W., Ma, Q., Thorne, R. M., Angelopoulos, V., Bortnik, J., et al. (2016). Direct evidence for EMIC wave scattering of relativistic electrons in space. *Journal of Geophysical Research: Space Physics*, *121*(7), 6620–6631. https://doi.org/10.1002/2016ja022521

Zhou, X., Gao, X., Lu, Q., Hajra, R., Ke, Y., Chen, R., & Ma, J. (2024). Prompt disappearance of magnetospheric chorus waves caused by high-speed magnetosheath jets. *Journal of Geophysical Research: Space Physics*, *129*(6), e2024JA032576. https://doi.org/10.1029/2024JA032576